Materials Advances

ROYAL SOCIETY OF CHEMISTRY

PAPER

View Article Online
View Journal | View Issue

Cite this: *Mater. Adv.*, 2021, 2, 7681

Received 15th May 2021,
Accepted 17th September 2021

DOI: 10.1039/d1ma00439e

rsc.li/materials-advances

Oxidative burst as a continuous H_2O_2 supplier for tumor oxygenation in photodynamic therapy†

Xianqing Shi,‡[a] Li Gui,‡[ab] Lin Zhou *[a] and Shaohua Wei *[ac]

Catalyzing H_2O_2 decomposition to generate O_2 can relieve tumor hypoxia, but the insufficient content of endogenous H_2O_2 limits its effect. Here, a nanomedicine consisting of Fe_3O_4 and zinc phthalocyanine (ZnPc12) was fabricated. In the tumor's normoxia zone, the photodynamic therapy (PDT) effect of ZnPc12 induces cancer cell's oxidative burst to generate massive endogenous H_2O_2. Fe_3O_4 catalyzes H_2O_2 decomposition to generate sufficient O_2 for PDT in the nearby hypoxia zone. It is the first time to utilize oxidative burst as a continuous H_2O_2 self-supplier for cancer treatment.

1. Introduction

Photodynamic therapy (PDT) is a clinical therapy strategy for cancer treatment. The photosensitizer (PS) will produce reactive oxygen species (ROS) to kill cancer cells post light irradiation at the tumor site in the presence of O_2.[1–4] Compared with other photosensitizer, zinc phthalocyanines were an 18-π electron conjugate composed of tetrapolypyrrole planar macrocycles. The outer periphery of the large ring was extended by a benzene ring, which enhanced its long-wavelength absorption and had a great application in PDT.[5,6] The hypoxic tumor microenvironment seriously hinders the therapeutic effect of PDT.[7–9] Catalyzing endogenous H_2O_2 decomposition to produce O_2 is a classic method to relieve tumor hypoxia.[10–12] Nevertheless, the above method's efficiency is restricted mainly by the low endogenous H_2O_2 in cancer cells (less than 100 μM).[13–16] Significantly, in cancer cells, the pericellular O_2 tension strongly influences endogenous H_2O_2 production, sharply decreasing under hypoxic conditions.[17] Thus, it is urgent to find an effective strategy to enhance endogenous H_2O_2 concentration.

Several strategies were reported to enhance endogenous H_2O_2 concentration. For example, glucose oxidase can catalyze glucose oxidation generating gluconic acid and H_2O_2;[18] some peroxide, such as CaO_2, CuO_2, or MgO_2, can react with H_2O to generate H_2O_2;[19] β-lapachone can cause a large number of intracellular H_2O_2 *via* a futile redox cycling;[20] $MoSe_2/CoSe_2$ can react with O_2 to generate H_2O_2 by a photocatalytic reaction.[21] Thus, co-delivery of these candidates with PS to cancer cells can effectively relieve tumor hypoxia to enhance the PDT outcome.

Oxidative burst was a typical response of plant cells in the physical or biological stress. The generation of ROS such as H_2O_2 was a symbol in plants during the oxidative burst.[22,23] The oxidative burst phenomenon was also found in immune cells or macrophages, which was infected by bacteria to release H_2O_2.[24–26] Tang and our group's previous reports found that the PDT damage could trigger the oxidative burst effect in cancer cells.[27,28] We found that such an effect significantly enhances the amount of endogenous H_2O_2, which could be an alternative H_2O_2 source for hypoxia relief. Normoxic and hypoxic zones both existed in solid tumors, depending on their distances with blood vessels. For example, breast cancer has severe O_2 gradients extending from ~50 mm Hg (7% O_2) to zero.[29] We proposed that such an oxidative burst could be utilized as a continuous H_2O_2 supplier to produce O_2 for cancer PDT treatment. In the tumor's normoxic zone, the PDT effect induced the cancer cell's oxidative burst to generate massive H_2O_2. Catalyzing H_2O_2 decomposition by a catalase or nanozyme can generate sufficient O_2 for PDT in the hypoxic zone nearby since O_2 is a small hydrophobic molecule that can be transported to hypoxic areas through a simple diffusion pathway along a concentration gradient.

To realize this vision, firstly, ZnPc with a satisfactory oxidative burst effect was selected. We synthesized twelve ZnPcs (ZnPc1–ZnPc12) with different side-chain structures and compared their oxidative burst effect post PDT treatment. Results indicated that ZnPc12 has the best oxidative burst effect

[a] College of Chemistry and Materials Science, Jiangsu Key Laboratory of Biofunctional Materials, Jiangsu Collaborative Innovation Centre of Biomedical Functional Materials, Key Laboratory of Applied Photochemistry, Nanjing Normal University, Nanjing, Jiangsu 210023, China. E-mail: zhoulin@njnu.edu.cn
[b] NanJing XiaoZhuang University, Nanjing, Jiangsu 210017, China
[c] School of Chemistry and Chemical Engineering, Yancheng Institute of Technology, Yancheng, Jiangsu 224051, China. E-mail: shwei@njnu.edu.cn

† Electronic supplementary information (ESI) available. See DOI: 10.1039/d1ma00439e

‡ X. Q. Shi and L. Gui contributed equally to the work.

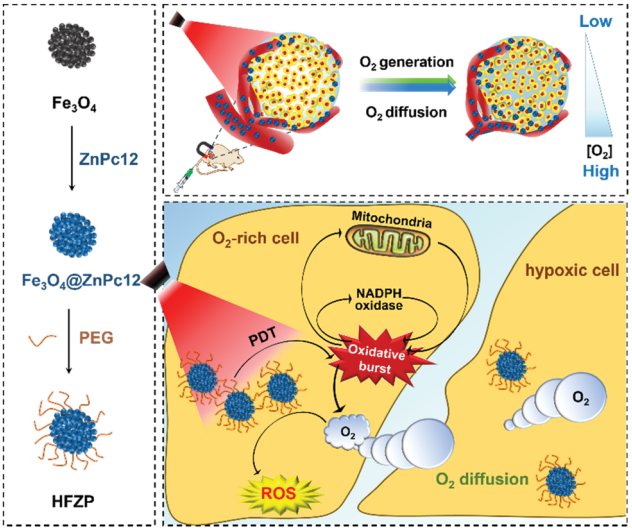

Fig. 1 The schematic presentation of the fabrication and anticancer mechanism of HFZP.

post-PDT treatment. Secondly, ZnPc12 has loaded in a histidine modified Fe_3O_4 aggregator, an excellent catalase-mimic nanozyme, and then encapsulated by polyethylene glycol (PEG) to form a stable nanocomplex (denoted HFZP) (Fig. 1). Fe_3O_4 integrates catalysis, magnetic targeting, and nuclear magnetic imaging (MRI) functions into one.[30,31] After the tail vein injection into mice, HFZP can accumulate at the tumor site assisted by a magnetic field and an enhanced permeability and retention (EPR) effect. Post light irradiation at the tumor tissue, the PDT process of ZnPc12 triggers the cancer cell's oxidative burst to produce abundant H_2O_2 at the tumor's normoxic zone. Moreover, Fe_3O_4 catalyzes H_2O_2 decomposition to generate sufficient O_2 for PDT in the nearby hypoxia zone for PDT outcome enhancement.

2. Experimental section

2.1 Cells and animals

The human cervical carcinoma cell line (HeLa) and murine mammary carcinoma cell line (4T1) were purchased from the Cell Bank of the Chinese Academy of Science (Shanghai, China). The cells were cultured in a conventional incubator (5% CO_2, 37°, for normoxia condition study) in DMEM based cell culture medium or a tri-gas incubator (5% CO_2, 5% O_2, 90% N_2, 37 °C, for hypoxia condition study) using N_2 saturated DMEM based cell culture medium. The female BALB/c nude mice (4–6 weeks) were purchased from the Center for Comparative Medicine of Yangzhou University. The animal experiments were conducted following the National Institute of Health Guide's guidelines for the Care and Use of Laboratory Animals. The Animal Ethics Committee approved all animal experiments of Nanjing Normal University (China).

2.2 H_2O_2 measurement of ZnPcs

BES–H_2O_2–Ac was a fluorescent probe, which was specific to H_2O_2. Tumor cells were incubated in 48-well plates for 24 h in an incubator (5% CO_2, 37 °C, for normoxia condition study). ZnPc1–ZnPc10 (5 μM) was added and incubated for another 4 h. The cells were irradiated by a 665 nm light-emitting diode (LED) for 5 min. After 3 h, the BES–H_2O_2–Ac probe (5 μM) was added in the cells for 1 h, and the cells were washed with phosphate-buffered saline (PBS) three times. And an inverted fluorescence microscope detected the fluorescence intensity of different ZnPcs. The H_2O_2 generation in different times of ZnPc4, ZnPc11, and ZnPc12 was detected in the following measurement. ZnPc4, ZnPc11, and ZnPc12 (5 μM) were added and incubated for 3 h. The BES–H_2O_2–Ac probe (5 μM) was added in cells for 1 h, and the cells were irradiated for 5 min. The fluorescence images were observed at 0 h. ZnPc4, ZnPc11, and ZnPc12 (5 μM) were added and incubated for 3 h. After irradiation for 5 min, the cells were incubated for another 11, 23, or 47 h. Then the BES–H_2O_2–Ac probe (5 μM) was added in cells for 1 h and the fluorescence images were observed at 12, 24, or 48 h using an inverted fluorescence microscope (the exposure time was 600 ms).

2.3 Safety and cytotoxicity detection of ZnPcs

Tumor cells were cultured in 96-well plates for 24 h in an incubator (5% CO_2, 37 °C, for normoxia condition study). ZnPc1–ZnPc10 (5 μM) was added with or without irradiated by a 665 nm light for 5 min after 4 h. For another 20 h, 10% 3-[4,5-dimethylthiazol-2-yl]-2,5-diphenyl tetrazolium bromide (MTT) was added and incubated for 4 h. Then, the original Dulbecco's minimum essential medium (DMEM) was removed, and dimethylsulfoxide (DMSO) was added to detect the optical density (OD) value at 570 nm using a microplate reader. The cell survival percent of ZnPc4, ZnPc11, and ZnPc12 in the dark and light cytotoxicity were also detected by the above method.

2.4 Preparation and characterization of HFZP

Fe_3O_4 was synthesized according to previous reports with the following procedures. $FeCl_3{\cdot}6H_2O$ (0.41 g), histidine (0.25 g), and sodium acetate (1.80 g) were dissolved in ethylene glycol (40 mL) by stirring and ultrasonic dispersing until it was clear. The above solution was then transferred into a Teflon-lined stainless-steel autoclave and reacted at 200 °C for 20 h. After cooling to room temperature, Fe_3O_4 was obtained and washed with ethanol five times and vacuum dried below 40 °C. Fe_3O_4 (5 μL, 12 mg mL^{-1}) and ZnPc12 (5 μL, 2 mg mL^{-1}) were mixed in water (5 mL) and ultrasonically dispersed for 15 min. ZnPc@Fe_3O_4 was obtained and then collected by centrifugation (the payload of ZnPc on Fe_3O_4 was 0.148 mg mg^{-1}). After that, ZnPc@Fe_3O_4 and PEG (5 μL, 50 mg mL^{-1}) were mixed in water (5 mL) and ultrasonically dispersed for 15 min. The result of HFZP was collected by centrifugation. The loading efficiency of ZnPc12 on HFZP was then calculated (the payload of ZnPc on HFZP was 0.037 mg mg^{-1}).

2.5 H_2O_2, O_2 and $^1O_2$ measurements

Tumor cells were incubated in 48-well plates for 24 h under normoxia conditions (5% CO_2, 37 °C). ZnPc12 and HFZP were added using an N_2 saturated DMEM based cell culture medium

and placed in a tri-gas incubator (5% CO_2, 5% O_2, 90% N_2, 37 °C, for hypoxia condition study). Other HFZP groups were added magnets for providing the magnetic field under the plates. The cells were incubated for another 3 h. After that, the cells were irradiated for 5 min and continued to be incubated for 23 h. Then BES–H_2O_2–Ac, Tris (4,7-diphenyl-1,10-phenanthroline)ruthenium(II) dichloride ($Ru(dpp)_3Cl_2$), and singlet oxygen sensor green (SOSG) probe (5 μM) were added to the cells. After 1 h, the cells were washed with PBS. The cells were irradiated for 5 min, and an inverted fluorescence microscope detected the fluorescence intensity of different drugs (the exposure times of the above probes were 800, 500, and 600 ms, respectively).

2.6 Antitumor activity *in vitro*

Tumor cells were cultured in 96-well plates for 24 h under normoxic conditions (5% CO_2, 37 °C). ZnPc12 (2.5 μM), Fe_3O_4 (34.05 mg L^{-1}), and HFZP (ZnPc: 2.5 μM, Fe_3O_4: 34.05 mg L^{-1}, PEG: 97.12 mg L^{-1}) were added using an N_2 saturated DMEM based cell culture medium and placed in a tri-gas incubator (5% CO_2, 5% O_2, 90% N_2, 37 °C, for hypoxia condition study). Other HFZP groups were added magnets for providing the magnetic field under the plates. The cells were irradiated by a 665 nm light for 5 min after 4 h. For another 20 h, 10% MTT was added and incubated for 4 h. Then, the original DMEM was removed, and DMSO was added and the OD value was detected using a microplate reader.

2.7 Apoptosis detection *in vitro*

Tumor cells were cultured in 6-well plates for 24 h under normoxia conditions (5% CO_2, 37 °C). ZnPc12, Fe_3O_4, and HFZP were added using an N_2 saturated DMEM based cell culture medium and placed in a tri-gas incubator (5% CO_2, 5% O_2, 90% N_2, 37 °C, for hypoxia condition study). Other HFZP groups were added magnets for providing the magnetic field under the plates. After irradiation for 5 min for incubating for another 24 h, DMEM culture solution was sucked out into the centrifuge tube, and the cells were washed with PBS and digested for appropriate time by tyrisin. The above DMEM was added to blow adherent cells and the cells were transferred to the centrifuge tube. Then the above cells were centrifuged at 1000 g for 5 min. The supernatant was removed and the cells were resuspended by PBS. After centrifugation again, the cells were collected and Annexin V-FITC binding solution was added to resuspend gently. After that, Annexin V-FITC (2.5 μL) and propidium iodide (PI, 5 μL) were added for blending. The cells were incubated at room temperature for 20 min in the dark and then detected using a flow cytometer (FCM).

2.8 Subcellular localization

HeLa cells were seeded in the confocal dish and incubated for 24 h. The original DMEM culture solution was removed and DMEM containing the drug (HFZP: 2 μM, calculated as ZnPc12) was added for another 4 h. Then the original medium was removed and the cells were washed with PBS. Lyso-tracker blue (75 nM) was added to the cells and cultured for 30 min. After that, the probe was taken out and the cells were washed with PBS. A confocal laser scanning microscope (CLSM) was used to obtain the fluorescence of Lyso-tracker blue and ZnPc12.

2.9 *In vivo* fluorescence imaging

4T1 cells (1×10^7 mL^{-1}) were subcutaneously injected (200 μL) in female BALB/c nude mice to establish bilateral tumor-bearing. When the tumor size reached approximately 100 mm^3, saline and HFZP solution (2.5 mg kg^{-1}, calculated as ZnPc12) were intravenously injected *via* the tail. The magnetic field was applied to the right-side tumor for 1 h. After 6 h, the mice were sacrificed to obtain the main organs, including heart, liver, spleen, lungs, kidneys, and tumor. The fluorescence distribution *in vivo* was measured by animal living imaging instrument (ALII) (E_x = 405 nm, E_m = 580–720 nm).

2.10 MRI measurements

[Fe] was a typical T_2 contrast agent and had a high relaxation rate (r). The relaxation rates of HFZP were detected to compare the contrast imaging effect. The concentration of [Fe] in HFZP was 0.019, 0.038, 0.076, 0.152, and 0.304 mM. The above samples were added to 1.5 mL centrifuge tubes and fixed with agarose, scanning using a low-field resonance imaging scanner at room temperature. The relaxation rate calculation formula is as follows:

$$\frac{1}{T} = \frac{1}{T_0} + r[\mathrm{Fe}]$$

where T_0 is the relaxation time of the agarose aqueous solution, T is the relaxation time of the test sample, [Fe] is the concentration HFZP, and r is the relaxation rate.

In this experimental section, the measurement conditions (T_2) were listed as follows: coil was selected 1#, TR was set to 2000, TE was set to 50 and average was set to 6. Then, T_2-MRI was measured in tumor-bearing mice before and after injecting HFZP (2.5 mg kg^{-1}). 1 h after administration, the magnetic field was added near one tumor position for 1 h. 6 h after injection, the mice were anesthetized for scanning.

2.11 Antitumor activity *in vivo*

The mice were randomly divided into 6 groups, and different treatments were given as follows: (1) control group: saline without light; (2) ZnPc12 + L group: 2.5 mg kg^{-1} with light; (3) Fe_3O_4 group: 16.89 mg kg^{-1} with light; (4) HFZP + M group: 2.5 mg kg^{-1} (calculated as ZnPc12) with the magnetic field and without light; (5) HFZP + L group: 2.5 mg kg^{-1} (calculated as ZnPc12) without a magnetic field and with light; and (6) HFZP + M + L group: 2.5 mg kg^{-1} (calculated as ZnPc12) with the magnetic field and with light. The samples were administered tail vein injection on days 1, 2, 3, 4, 5, 6, 7, 8, 10, and 13. After injection for 1 h, the HFZP + M and HFZP + M + L groups were added magnets for providing the magnetic field in the tumor for 1 h. After injection for 6 h, ZnPc12, HFZP + L, and HFZP + M + L groups were irradiated by a 665 nm LED light for 30 min. The weight and tumor volume were recorded every day. After treatment for 14 days, the

mice were sacrificed to obtain the main organs and tumor sections for H&E staining analysis.

2.12 Immunofluorescence detection

The mice were treated with the above antitumor activity *in vivo* conditions. Then pimonidazole hypoxyprobe-1 (60 mg kg^{-1}) was administrated in mice by intraperitoneal injection. 90 minutes later, the tumor was taken out and embedded with an optimal cutting temperature compound (OCT) embedding medium for the frozen section. The obtained slices were placed in precooled acetone at 4 °C and fixed for 15 min. Then the slices were taken out and washed with PBS (1×) 3 times, and the slices were gently shaken for 10 min each time. After that, the slices were placed in PBS (1×) containing 0.2% TX-100 for 15 min and washed with PBS (1×) 3 times. The tissues were painted with a histochemical pen, and the sealing solution (goat serum) was added to the tissue in the circle of the histochemical pen for incubating for 1 h in the dark. The obtained sections were incubated with the mouse IgG1 primary antibody (1 : 150, v-v) and CD 31 antibody (1 : 200, v-v) overnight at 4 °C. After the slices were removed and restored to room temperature, they were cleaned with PBS (1×) 3 times and gently shaken for 10 min each time. The secondary antibody rabbit IgG (1 : 150, v-v) was added for incubating for 1 h in the dark, and the fluorescence images were observed using CLSM.

2.13 Fe^{2+} release detection of Fe_3O_4

The measurement of the standard curve: *o*-phenanthroline was a color agent that could combine Fe^{2+} to form the red complex. According to the Lambert–beer law ($A = \varepsilon bc$), the concentration of Fe^{2+} could be calculated. $FeCl_3$ (1 mg mL^{-1}) was respectively taken out in 0, 10, 20, 30, 40, and 50 μL and added in the aqueous solution (3 mL), and then 0.15% *o*-phenanthroline (300 μL) and 10% hydroxylamine hydrochloride (100 μL) were added to the mixture solution. After reacting for 2 min, different Fe^{2+} concentrations corresponding to the UV-Vis spectrum were detected and the standard curve was calculated.

The measurement of Fe^{2+} release: the samples were divided into 8 groups, and different treatments were given as follows: (1) 0 h – H_2O_2: 3 mL aqueous solution (pH = 4.5) + 15 μL Fe_3O_4 (10 mg mL^{-1}), the above solution was mixed and centrifuged immediately. The supernatant was collected for detection. (2) 0 h + H_2O_2: 3 mL aqueous solution (pH = 4.5) + 15 μL Fe_3O_4 (10 mg mL^{-1}) + 30 μL H_2O_2 (100 mM), the above solution was mixed and centrifuged immediately. The supernatant was collected for detection. (3–8) 24 h, 48 h, 72 h, 96 h, 120 h and 144 h + H_2O_2: 3 mL aqueous solution (pH = 4.5) + 15 μL Fe_3O_4 (10 mg mL^{-1}) + 30 μL H_2O_2 (100 mM), the above solution was mixed and centrifuged every day respectively at the same time. The supernatant was collected for detection. After that, 0.15% *o*-phenanthroline (300 μL) and 10% hydroxylamine hydrochloride (100 μL) were added to the above supernatant. After reacting for 2 min, the maximum absorbance at 510 nm was measured using the UV-Vis spectrum.

3. Results and discussion

3.1. Oxidative burst effect by ZnPcs

The substitution group of ZnPc could strongly influence its properties. Therefore, ten ZnPcs (ZnPc1–ZnPc10) with various substitution groups were chosen for the study (the synthetic routes of the ZnPcs are given in the ESI,† and their structures are shown in Fig. S1–S5†). The BES–H_2O_2–Ac probe, which could interact with H_2O_2 specifically to generate the fluorescent product DFF with bright green fluorescence, was used to detect the H_2O_2 concentration enhancement post the PDT process of the above ZnPcs.[32]

The concentration of ZnPcs was chosen as 5 μM since there is no apparent dark cytotoxicity of these ZnPcs at this concentration (Fig. S6, ESI†). Post 665 nm light irradiation for 5 min and incubation in the dark for 24 h, the brightest DFF green fluorescence was detected in the cells treated with ZnPc4 (Fig. S7, ESI†). This phenomenon proves that ZnPc4 could effectively induce oxidative burst to generate H_2O_2 post the PDT process, and the benzoic acid group substitution could help this effect. Thus, ZnPc11 and ZnPc12 with more benzoic acid group substitution were synthesized, and their oxidative burst effect was compared (Fig. 2B). After PDT treatment, the DFF fluorescence intensity of ZnPc12-treated cells was the strongest, indicating that its oxidative burst induced H_2O_2 generation amount is higher than those of ZnPc4 and ZnPc11. Besides, ZnPc12 has satisfactory light-toxicity to the cancer cells under normoxic conditions (Fig. S8, ESI†). Thus, ZnPc12 was selected for the following study in this paper.

3.2. The mechanism of oxidative burst

H_2O_2 can be directly generated by the type I mechanism of the PDT.[33] As shown in Fig. 2B1, trace H_2O_2 generated post light irradiation immediately, which is referred to as 0 h after irradiation, indicates that the type I PDT is not the primary source of H_2O_2 in the oxidative burst. Endogenous H_2O_2 of the cell can be generated by the mitochondrial respiratory chain and NADPH oxidase. To prove that the endogenous H_2O_2 generation is a critical source of the oxidative burst, the mitochondrial respiratory chain complex II inhibitor, thenoyltrifluoroacetate (TTFA),[34] and an NADPH oxidase inhibitor, apocynin,[35] were used. As shown in Fig. 3A, adding TTFA or apocynin decreased DFF's green fluorescence intensity sharply, indicating that mitochondrial respiratory chain and NADPH oxidase dysfunction inhibits the oxidative burst of ZnPc12. The results indicated that in addition to the PDT type I mechanism, the mitochondrial respiratory chain and NADPH oxidase influence by the PDT process of ZnPc12 participated in the endogenous H_2O_2 production to induce the H_2O_2 burst.

ZnPc12 was localized in the lysosome (Fig. 3B1). How does it influence the mitochondrial respiratory chain and NADPH oxidase located at the mitochondria and membrane, respectively? Therefore, the PDT damage process caused by light started from the lysosome. Endogenous H_2O_2 in tumor cells was mainly produced in mitochondria.[36,37] ROS generation in the lysosome changed the lysosomal membrane permeabilization (LMP), which

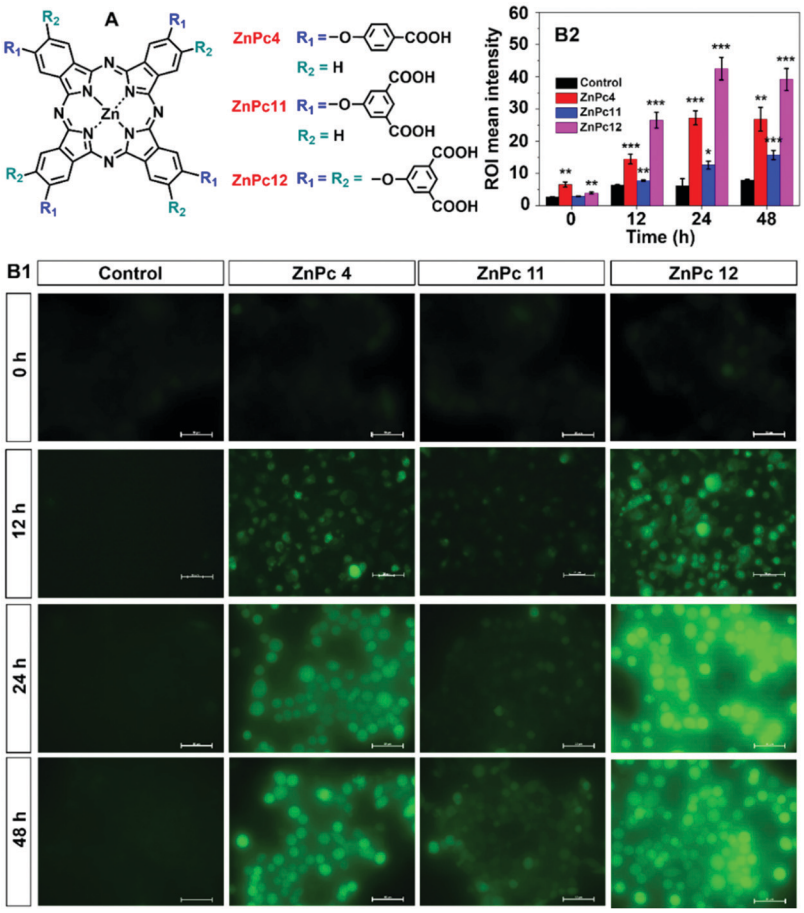

Fig. 2 (A) The structures of ZnPc4, ZnPc11, and ZnPc12; (B1) DFF fluorescence signal and (B2) intensity comparison from ZnPc4, ZnPc11, or ZnPc12 treated cells post light irradiation and incubation for 0 h, 12 h, 24 h or 48 h in the dark (bar = 50 μm) (*$P < 0.05$, **$P < 0.01$, ***$P < 0.001$ ZnPcs treated groups *versus* control).

was verified by the acridine orange (AO) release experiment (Fig. 3B2). LMP induced protease was released into the cytoplasm to influence the NADPH oxidase and mitochondrion membrane permeabilization (MMP), which was verified by Rhodamine-123 (Rh 123) experiment (Fig. 3B3). MMP could result in mitochondrial dysfunction to influence the respiratory chain.[38,39]

In summary, there are direct and indirect H_2O_2 sources in the oxidative burst. The direct H_2O_2 source is from the type I mechanism of the PDT. After the injury by the ROS generated by PDT, the dysfunction of the mitochondrial respiratory chain and the NADPH oxidase caused indirect H_2O_2 production is the indirect H_2O_2 sources in the oxidative burst (Fig. 3C).

3.3. Fabrication and properties of HFZP

The histidine modified ultra-small Fe_3O_4 aggregator is prepared by a modified hydrothermal method, and the histidine modification is proved by the XPS spectra (Fig. S10, ESI†). After loading ZnPc12, no noticeable morphology changes were detected for Fe_3O_4 (Fig. 4A1 and A2). The payload of ZnPc12 on Fe_3O_4 was 0.148 mg mg^{-1}. Furthermore, PEG was encapsulated on the surface of Fe_3O_4@ZnPc12 to obtain HFZP and the payload of ZnPc12 on HFZP was 0.037 mg mg^{-1}. After being encapsulated by PEG, a transparent layer appeared around the nanoparticles (Fig. 4A3), and its average size was 183.6 nm (Fig. S11, ESI†). More importantly, dynamic light scattering (DLS) patterns in different physiological solutions (including saline, PBS, and DMEM) were also detected and there was no obvious HFZP aggregation (Fig. S12, ESI†). After loading ZnPc12 on the surface of positively charged Fe_3O_4, the zeta potential was decreased to −16.93 mV. The negatively charged PEG encapsulation made the zeta potential of HFZP to be −25.9 mV (Fig. S13, ESI†). It is indicated that ZnPc12 and PEG were effectively loaded onto Fe_3O_4. HFZP can be well dispersed in the aqueous solution, while HFZP moves to the magnet's position after adding the magnet, proving that HFZP has satisfactory magnetism (Fig. S14, ESI†). In the solution of Fe_3O_4 or HFZP solution in the presence of H_2O_2, massive O_2 was generated, proving the catalase-mimic function of Fe_3O_4 (Fig. 4B). The ultrathin section of the cells treated with HFZP was observed by TEM to prove that HFZP can be effectively taken up by cancer cells (Fig. S15, ESI†). HFZP was located at the lysosome, which was proved by co-treating the cancer cells by HFZP and Lyso-tracker blue (Fig. S16, ESI†).

The following *in vitro* experiments were carried out under hypoxic conditions in the tri-gas incubator (5% CO_2, 5% O_2, 90% N_2). The detected H_2O_2, O_2 and $^1O_2$ were used as BES–H_2O_2–Ac, $Ru(dpp)_3Cl_2$, and SOSG probes, respectively. As shown in Fig. 4C, BES–H_2O_2–AC is a kind of fluorescent probe specific for H_2O_2.[40] Compared to the cells treated with ZnPc12,

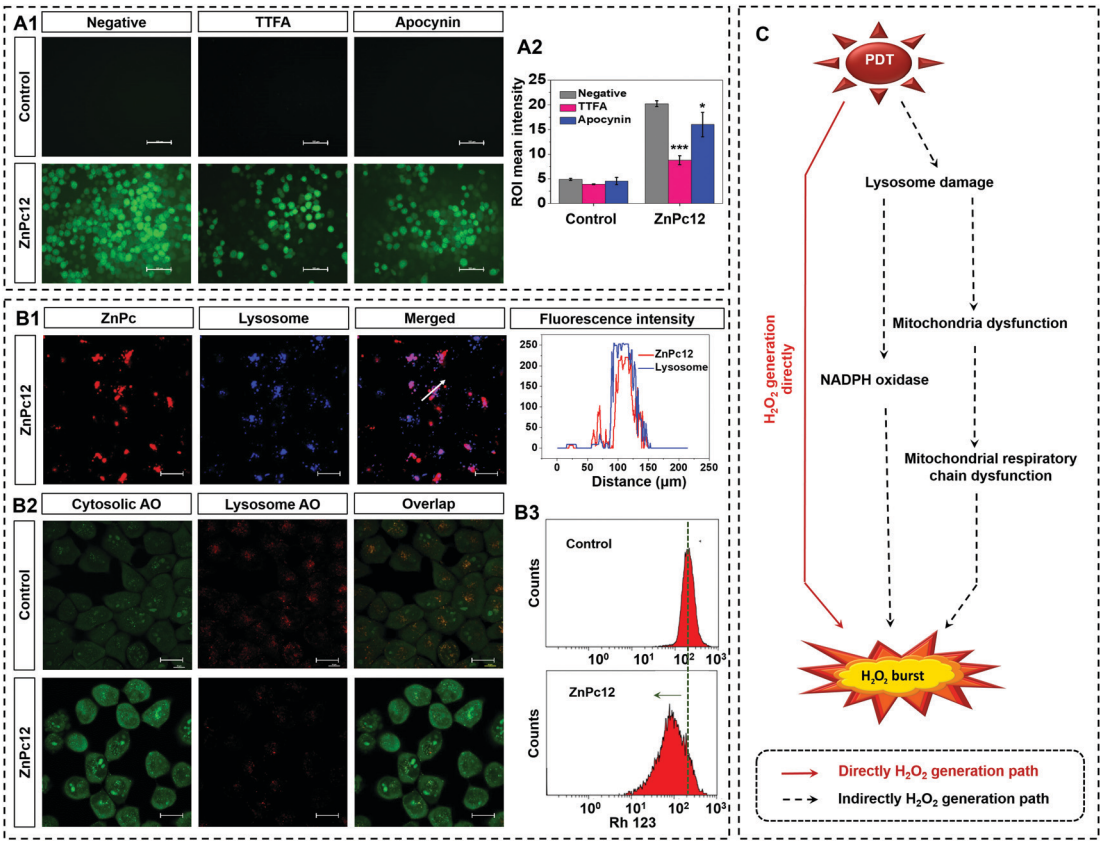

Fig. 3 (A) Fluorescence images and intensity comparison of oxidative burst by TTFA and apocynin inhibitor pretreatment (bar = 100 μm). (B1) Subcellular localization was detected by ZnPc12 using a lysosome probe (bar = 20 μm). Lysosome membrane permeability and mitochondrial membrane potential were measured by AO (B2) and Rh 123 staining (B3) (bar = 20 μm). (C) The mechanism of ZnPc12 induced oxidative burst post the PDT process.

the H_2O_2 concentration in the cells treated with HFZP was decreased, indicating the decomposition of H_2O_2 catalyzed by HFZP in these cells. $Ru(dpp)_3Cl_2$ was widely used as a probe for luminescence detection and oxygen quantitative determination. The fluorescence intensity of $Ru(dpp)_3Cl_2$ (absorbance λ_{max} = 455 nm, emission λ_{max} = 613 nm) was significantly reduced by O_2 due to quenching and it is an effective oxygen probe based on strength or decay time measurements.[41] In contrast, the intracellular O_2 concentration in the cells treated with HFZP was higher than that in ZnPc12 treated cells, indicating effective O_2 generation from H_2O_2 decomposition. Moreover, compared with the cells treated with HFZP but without a magnetic field, the cells treated with HFZP with a magnet (HFZP + M) showed more obvious H_2O_2 decomposition and O_2 generation since the magnetic field could promote HFZP uptake by cancer cells (Fig. 4C). SOSG was used as an indicator to evaluate $^1O_2$ production in different groups.[42] Compared to the cells treated with ZnPc12, the $^1O_2$ concentration in the cells treated with HFZP was increased. The results showed that HFZP could produce $^1O_2$ effectively and had better activity in a complicated physiological environment. The *in vitro* antitumor activity of HFZP was researched by MTT assay. Compared to ZnPc12, the light-toxicity of HFZP was enhanced under hypoxic conditions. Moreover, under the magnetic field, the PDT activity of HFZP was further improved (Fig. 4D). Besides, the cell apoptosis of the drugs was also detected by FCM. The apoptotic ratio of HFZP + M was 83.61%, superior to those of the other groups (Fig. 4E and Fig S17, ESI†).

3.4 *In vivo* bio-distribution and MRI imaging of HFZP

The *in vivo* HFZP distribution was detected using a bilateral tumor-bearing mice model. One side of the tumor has put a magnet to provide the magnetic field (HFZP + M side) to evaluate the magnetic field assisted targeting ability of HFZP, and another side has not put the magnet (HFZP side). HFZP could effectively accumulate at the tumor tissue. Moreover, the HFZP + M side fluorescence intensity was more robust than the HFZP side in bearing bilateral tumor mice, indicating the magnetic field assisted targeting function of HFZP (Fig. 5A).

T_2-MRI is a susceptible technology to detect cancer. To create a T_2-weighted image, magnetization is allowed to decay before measuring the MRI signal by changing the echo time. T_2-Weighted image weighting is appropriate for detecting water-rich pathological tissue, such as tumors, edema, and inflammation. Fe-containing nanomaterials can be used as T_2 contrast agents. Therefore, with the increasing concentration of HFZP, the T_2-weighted MRI signal intensity was gradually decreased, which demonstrated the targeting abilities of HFZP.[43] The inset panel in Fig. 5B2 showed an increase in the T_2-MRI signal strength of HFZP with an increase in the Fe

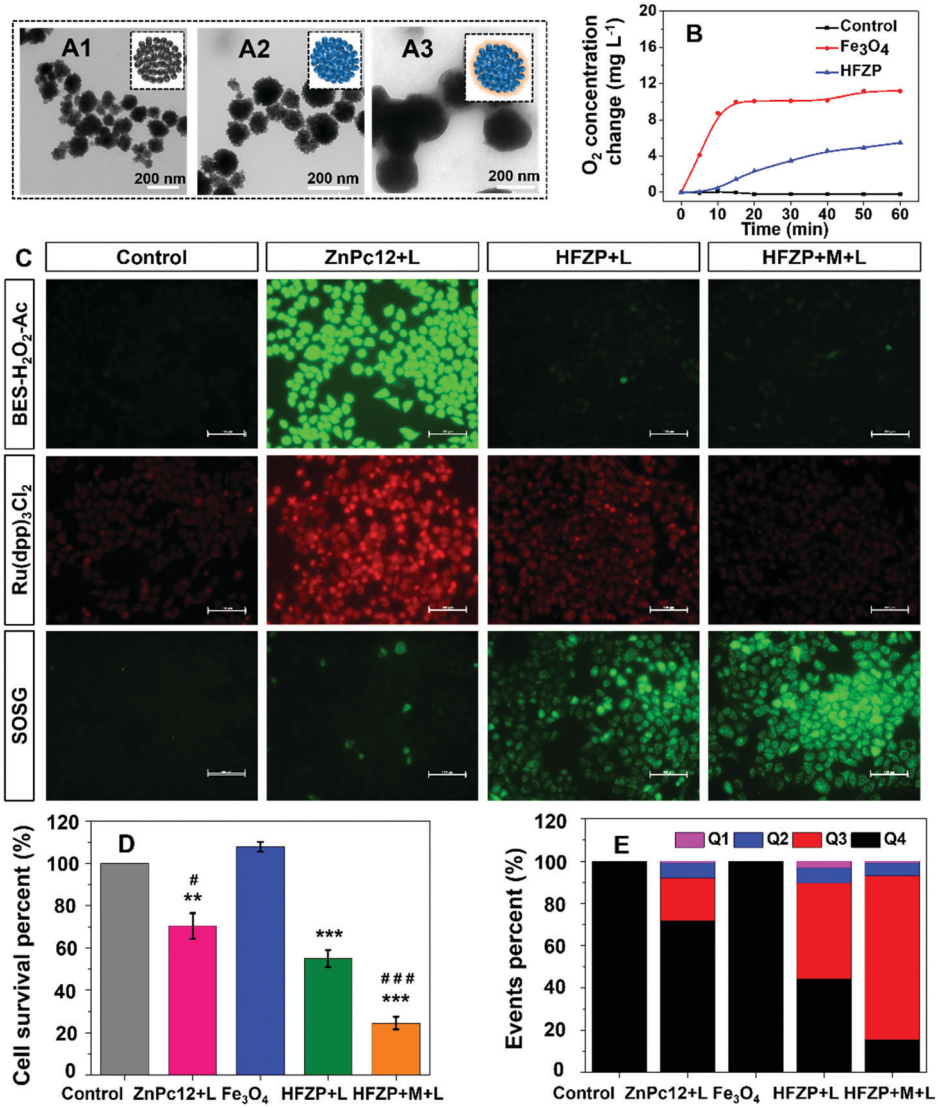

Fig. 4 TEM image of Fe_3O_4 (A1), Fe_3O_4@ZnPc (A2) and HFZP (A3). (B) O_2 generation comparison in aqueous, Fe_3O_4 and HFZP solution for 60 min (H_2O_2: 20 mM). (C) Comparison of fluorescence images of H_2O_2, O_2 and $^1O_2$ was observed by BES–H_2O_2–Ac, $Ru(dpp)_3Cl_2$, and SOSG probes (bar = 100 μm). (D) The light cytotoxicity comparison of Control, ZnPc12 + L, Fe_3O_4, HFZP + L and HFZP + M + L (**$P < 0.01$, ***$P < 0.001$ drugs treated *versus* control; #$P < 0.05$, ###$P <$ 0.001 ZnPc12 + L and HFZP + L *versus* HFZP + L). (E) Cell apoptosis quantitative analysis of control, ZnPc12 + L, Fe_3O_4, HFZP + L and HFZP + M + L by FCM.

concentration, proving that HFZP is an ideal T_2-MRI regent. The relaxation rate (r) of HFZP was 147.2 mM^{-1} S^{-1}. As shown in Fig. 5B1 and B3, before injection, there was no magnetic material [Fe] and so there was a strong MRI signal in the tumor. However, the MRI signal decreased because of the magnetization effect of [Fe] and [Fe] was contained within the HFZP. Therefore, 6 h post-injection of HFZP, the T_2-MRI signals showed a sharp decrease in the tumor, which also indicates the targeting ability of HFZP. With the assistance of the magnetic field, the tumor tissue's T_2-MRI signal was further decreased, indicating the magnetic field assisted targeting ability of HFZP.

3.5 The depth of tumor penetration and tumor suppression functions

The blood supply of the solid tumor is insufficient, resulting in the tumor cells close to the blood vessels being normoxic, and most tumor cells far away from the blood vessels being hypoxic.[44,45]

The CD 31 antibody was used to label the blood vessels in tumor tissue. The hypoxic probe (pimonidazole hypoxyprobe-1) was applied to observe the O_2 concentration at the tumor tissue post-treatment by various drugs. The bright green fluorescence of pimonidazole hypoxyprobe-1 can be effectively enhanced under hypoxic conditions but quenched by O_2 under well-oxygenated conditions. As shown in Fig. 6A, in the solid tumor of the mice without any treatment, the green fluorescence signal intensity of the normoxic zone (around the blood vessel) was weak, and the fluorescence signal intensity of the hypoxic zone (far away from the blood vessel) was vigorous. In the solid tumor of ZnPc12 treatment mice, the green fluorescence signal intensity was enhanced overall even around blood vessels, demonstrating that O_2 was consumed during the PDT process

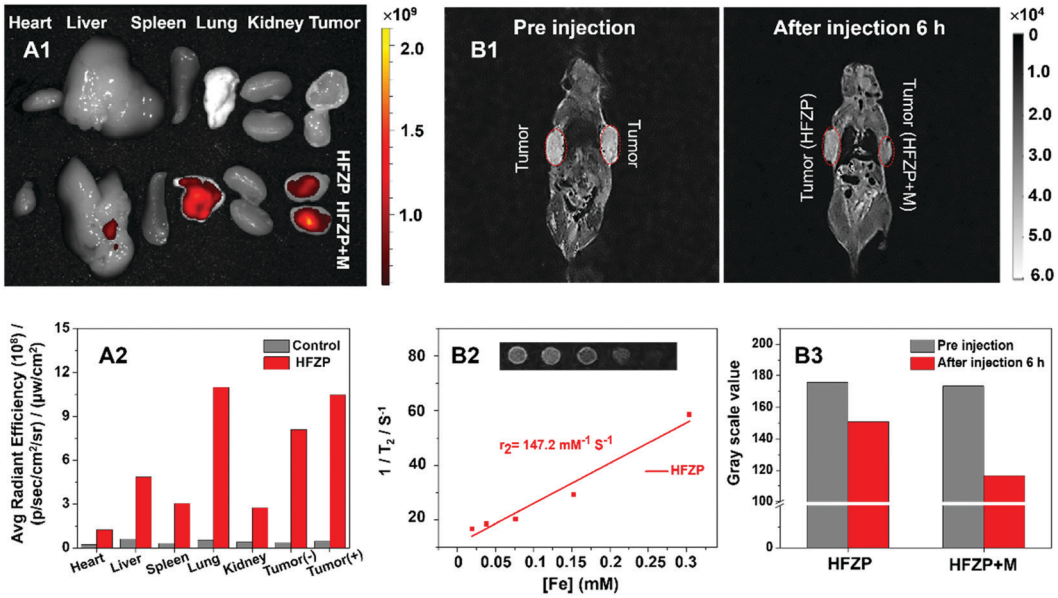

Fig. 5 (A) *In vivo* fluorescence images and intensity of main organs and tumors pre injection and after injection HFZP without or with a magnet. T_2-weighted MRI images (B1) and gray value (B3) of bilateral tumor bearing mice by HFZP and HFZP + M post tail vein injection at 0 and 6 h. (B2) Linearity curve of r_2 ($1/T_2$) *versus* [Fe] of corresponding relaxivity. The inset shows T_2-weighted MRI images by different [Fe] concentrations in HFZP.

of ZnPc12. In contrast, the hypoxia was efficiently relieved overall in the solid tumor zones, both near and far away from the blood vessel, of the HFZP group. These data proved that in the tumor normoxic zone, the PDT effect of ZnPc12 in HFZP induces cancer cell oxidative burst to generate massive endogenous H_2O_2. Then, Fe_3O_4 in HFZP catalyzes H_2O_2 decomposition to generate sufficient O_2 for PDT in the nearby hypoxia zone.

Then *in vivo* biological safety and tumor suppression activity of ZnPc12, Fe_3O_4, and HFZP under the different conditions were studied further. As shown in Fig. S18A (ESI†), all mice treated with various drugs under different conditions did not

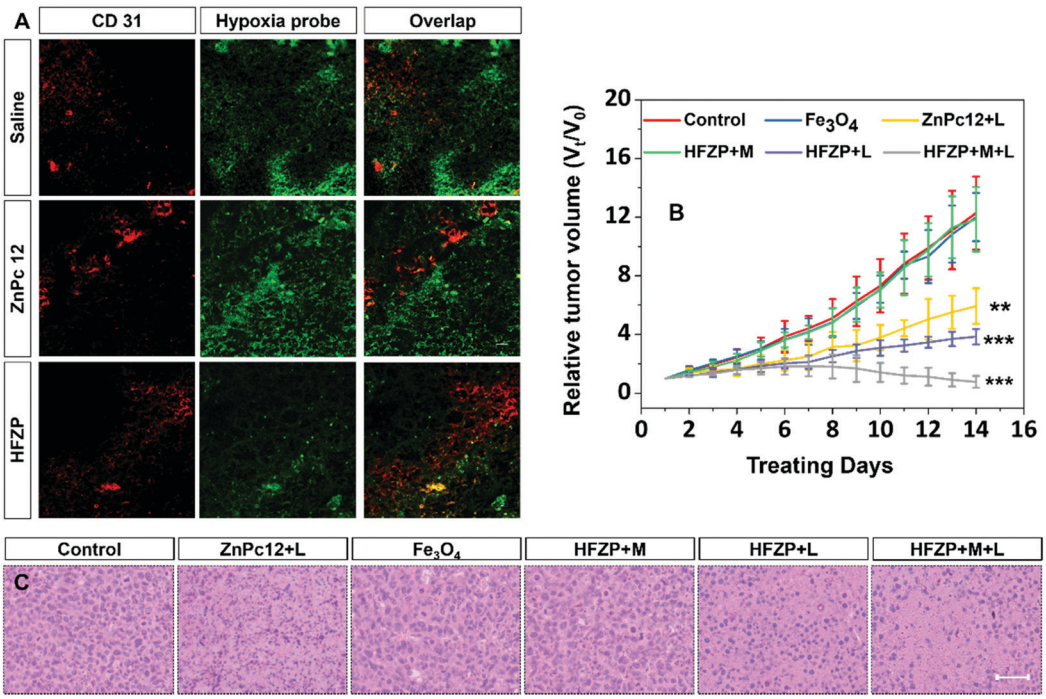

Fig. 6 (A) Immunofluorescence staining images of tumor tissue from control, ZnPc12, and HFZP groups using the CD 31 antibody and hypoxia probe labeling. (B) Relative tumor volume (V_t/V_0) during 14 days therapy of various drugs treated mice (**$P < 0.01$, ***$P < 0.001$ drugs treated *versus* control). (C) H&E staining of tumor tissue sections from the mice post different strategy treatments (bar = 50 μm).

show noticeable weight loss. After treatment for 14 days, no histopathological damage was detected in the main organs from the H&E staining of these tissues' sections. These results indicated that ZnPc12, Fe_3O_4, and HFZP had excellent biocompatibility *in vivo* (Fig. S18B, ESI†).

Compared with the control group, Fe_3O_4 and HFZP + M groups did not show apparent tumor suppression. In contrast, the tumor growth of ZnPc12 + L, HFZP + L, and HFZP + M + L groups was significantly inhibited. The *in vivo* PDT activity of HFZP was superior to that of ZnPc12, and the magnetic field assisted tumor-targeting ability further enhances the PDT outcome of HFZP (Fig. 6B). The H&E staining results of tumor sections also prove these conclusions, and the HFZP + M + L group induced the most severe nuclear damage in all groups (Fig. 6C). The above data proved that HFZP has practical magnetic field-assisted tumor targeting ability and satisfactory *in vivo* PDT-induced tumor suppression activity.

It could also be observed that HFZP disaggregated into ultrasmall particles with an average size of 8.77 nm (Fig. S19A1 and A2, ESI†) in the presence of H_2O_2. Furthermore, most HFZP nanoparticles were disaggregated in the cells treated with HFZP for 24 h post-light irradiation (Fig. S19B, ESI†). Such a change was mainly due to the H_2O_2 burst-induced HFZP nanoparticle disaggregation.

Furthermore, we added the release capacity of Fe^{2+} from the HFZP solution in the absence or presence of H_2O_2. Fe^{2+} release from HFZP under acidic conditions (pH = 4.5) was detected by o-phenanthroline colorimetry.[46] The standard curve of Fe concentration was measured, and the linear equation was fitted $y = 0.0568x + 0.0162$ (Fig. S19C and D, ESI†). As shown in Fig. S19E (ESI†), Fe concentrations in supernatants were calculated to be 0.04, 0.37, 2.92, 3.81, 3.75, 3.95, 4.09, and 3.91 μg mL^{-1} by the standard curve at the different times, respectively. It was indicated that Fe^{2+} release from HFZP gradually increased with the prolonging incubation times in an aqueous acid solution in the presence of H_2O_2. The maximum release content of 74.09% was reached. We proposed that the disaggregation and dissolution of HFZP are conducive to its metabolism.

Just as the references mentioned, the clearance of Fe_3O_4-based materials in our body is always through the liver.[47] In order to observe more intuitively the effects of HFZP on the liver of mice, H&E staining of main organs was performed. It could be seen that the liver was expected and no lesion performance occurs, which further demonstrates the safety of HFZP to the liver.[48,49]

4. Conclusions

Catalyzing endogenous H_2O_2 decomposition to generate O_2 can relieve tumor hypoxia and enhance PDT activity. However, the endogenous H_2O_2 content is inadequate. Moreover, the pericellular O_2 tension strongly influences the endogenous H_2O_2 production, significantly decreasing under hypoxic conditions. Here, we found that the PDT process of ZnPc12 induced cancer cell oxidative burst to generate massive H_2O_2, which can be an alternative H_2O_2 supplier to relieve tumor hypoxia. Then, HFZP consisting of ZnPc12, Fe_3O_4, and PEG was fabricated. In the tumor normoxia zone, cancer cell oxidative burst by ZnPc12 provides massive H_2O_2. Fe_3O_4 catalyzes H_2O_2 decomposition to generate sufficient O_2 for PDT in the hypoxia zone nearby since O_2 is a small hydrophobic molecule that can be transported to hypoxic areas through a simple diffusion pathway along a concentration gradient. Thus, we proposed that the oxidative burst is a continuous H_2O_2 self-supplier, which could be utilized for hypoxia relief in research areas including but not limited to cancer PDT treatment.

Author contributions

Xianqing Shi: design, fabrication, property identification of nanomedicine, and writing. Li Gui: *in vitro* and *in vivo* bioactivity research, ROS detection, and cell and animal imaging. Lin Zhou: design and revision. Shaohua Wei: revision and providing funds.

Conflicts of interest

There are no conflicts to declare.

Acknowledgements

X. S. and L. G. contributed equally to the work. This research was supported financially by the National Natural Science Foundation of China (21671105), the Priority Academic Program Development of Jiangsu Higher Education Institutions, the Foundation of Jiangsu Collaborative Innovation Centre of Biomedical Functional Materials (161090H001), and the Postgraduate innovation Project of Jiangsu Province (181200002470).

References

1 J. Ji, X. Li, T. Wu and F. Feng, *Chem. Sci.*, 2018, **9**, 5816–5821.
2 J. Karges, U. Basu, O. Blacque, H. Chao and G. Gasser, *Angew. Chem., Int. Ed.*, 2019, **58**, 14334–14340.
3 G. Z. Li, S. M. Yuan, D. S. Deng, T. Ou, Y. Q. Li, R. Sun, Q. F. Lei, X. S. Wang, W. W. Shen, Y. Y. Cheng, Z. Liu and S. Wu, *Adv. Funct. Mater.*, 2019, **29**, 1901932.
4 N. Tian, W. Z. Sun, X. S. Guo, J. Lu, C. Li, Y. J. Hou, X. S. Wang and Q. X. Zhou, *Chem. Commun.*, 2019, **55**, 2676–2679.
5 X. Li, B. D. Zheng, X. H. Peng, S. Z. Li, J. W. Ying, Y. Zhao, J. D. Huang and J. Yoon, *Coord. Chem. Rev.*, 2019, **379**, 147–160.
6 X. Li, J. F. Lovell, J. Yoon and X. Chen, *Nat. Rev. Clin. Oncol.*, 2020, **17**, 657–674.
7 X. Li, N. Kwon, T. Guo, Z. Liu and J. Yoon, *Angew. Chem., Int. Ed.*, 2018, **57**, 11522–11531.
8 S. Kuang, L. L. Sun, X. R. Zhang, X. X. Liao, T. W. Rees, L. L. Zeng, Y. Chen, X. T. Zhang, L. N. Ji and H. Chao, *Angew. Chem., Int. Ed.*, 2020, **59**, 20679–20703.
9 X. H. Wang, X. Y. Wang, S. X. Jin, N. Muhammad and Z. J. Guo, *Chem. Rev.*, 2019, **119**, 1138–1192.

10 X. Yang, Y. Yang, F. Gao, J. J. Wei, C. G. Qian and M. J. Sun, *Nano Lett.*, 2019, **19**, 4334–4342.
11 J. H. Liang, Y. Zheng, X. W. Wu, C. P. Tan, L. N. Ji and Z. W. Mao, *Adv. Sci.*, 2020, **7**, 1901992.
12 Y. Ding, Z. Y. Song, Q. Liu, S. H. Wei, L. Zhou, J. H. Zhou and J. Shen, *Dalton Trans.*, 2017, **46**, 11875–11883.
13 S. Dong, Y. Chen, L. Yu, K. Lin and X. Wang, *Adv. Funct. Mater.*, 2019, **30**, 1907071.
14 Z. Wang, B. Liu, Q. Sun, S. Dong, Y. Kuang, Y. Dong, F. He, S. Gai and P. Yang, *ACS Appl. Mater. Interfaces*, 2020, **12**, 17254–17267.
15 S. Gao, P. Zheng, Z. Li, X. Feng, W. Yan, S. Chen, W. Guo, D. Liu, X. Yang, S. Wang, X. J. Liang and J. Zhang, *Biomaterials*, 2018, **178**, 83–94.
16 D. W. Zheng, B. Li, C. X. Li, J. X. Fan, Q. Lei, C. Li, Z. Xu and X. Z. Zhang, *ACS Nano*, 2016, **10**, 8715–8722.
17 J. Fandrey, S. Frede and W. Jelkmann, *Biochem. J.*, 1994, **303**, 507–510.
18 M. Lyu, D. Zhu, X. Kong, Y. Yang, S. Ding, Y. Zhou, H. Quan, Y. Duo and Z. Bao, *Adv. Healthcare Mater.*, 2020, **9**, 1901819.
19 H. Hu, L. Yu, X. Qian, Y. Chen, B. Chen and Y. Li, *Adv. Sci.*, 2020, **8**, 2000494.
20 S. Wang, G. Yu, Z. Wang, O. Jacobson, L. S. Lin, W. Yang, H. Deng, Z. He, Y. Liu, Z. Y. Chen and X. Chen, *Angew. Chem., Int. Ed.*, 2019, **58**, 14758–14763.
21 Y. Li, R. Jia, H. Lin, X. Sun and F. Qu, *Adv. Funct. Mater.*, 2020, **31**, 2008420.
22 J. Wu and X. Ge, *Biotechnol. Bioeng.*, 2004, **85**, 714–721.
23 G. P. Bolwell, D. R. Davies, C. Gerrish, C.-K. Auh and T. M. Murphy, *Plant Physiol.*, 1998, **116**, 1379–1385.
24 P. Yang, S. Huang and A. Xu, *Amphioxus Immunity*, 2016, 153–165, DOI: 10.1016/b978-0-12-849903-0.00008-7.
25 J. M. Slauch, *Mol. Microbiol.*, 2011, **80**, 580–583.
26 J. B. Bliska and D. S. Black, *Infect. Immun.*, 1995, **63**, 681–685.
27 T. Wang, J. Hu, H. Luo, H. Li, J. Zhou, L. Zhou and S. Wei, *Small*, 2018, **14**, 1802337.
28 Z. Yu, Q. Sun, W. Pan, N. Li and B. Tang, *ACS Nano*, 2015, **9**, 11064–11074.
29 G. L. Semenza, *Mol. Aspects Med.*, 2016, **47-48**, 15–23.
30 B. Li, T. Gong, N. Xu, F. Cui, B. Yuan, Q. Yuan, H. Sun, L. Wang and J. Liu, *Small*, 2020, **16**, 2003969.
31 Y. Yao, D. Zhao, N. Li, F. Shen, J. O. Machuki, D. Yang, J. Li, D. Tang, Y. Yu, J. Tian, H. Dong and F. Gao, *Anal. Chem.*, 2019, **91**, 7850–7857.
32 X. Jiang, H. Wang, R. Yuan and Y. Chai, *Anal. Chem.*, 2018, **90**, 8462–8469.
33 Y. Y. Wang, Y. C. Liu, H. W. Sun and D. S. Guo, *Coord. Chem. Rev.*, 2019, **395**, 46–62.
34 T. Nishikawa, D. Edelstein, X. L. Du, S.-I. Yamagishi, T. Matsumura, Y. Kaneda, M. A. Yorek, D. Beebe, P. J. Oates, H.-P. Hammes, I. Giardino and M. Brownlee, *Nature*, 2000, **404**, 787–790.
35 L. Y. Hou, F. Q. Sun, R. X. Huang, W. Sun, D. Zhang and Q. S. Wang, *Redox Biol.*, 2019, **22**, 101134.
36 J. Sun, K. Du, J. J. Diao, X. T. Cai, F. D. Feng and S. Wang, *Angew. Chem., Int. Ed.*, 2020, **59**, 12122–12128.
37 G. Q. Yang, Z. J. Liu, R. L. Zhang, X. H. Tian, J. Chen, G. M. Han, B. H. Liu, X. Y. Han, Y. Fu, Z. J. Hu and Z. P. Zhang, *Angew. Chem., Int. Ed.*, 2020, **59**, 16154–16160.
38 C. Marques, C. S. Oliveira, S. Alves, S. R. Chaves, O. P. Coutinho, M. Corte-Real and A. Preto, *Cell Death Dis.*, 2013, **4**, 507.
39 K. Xu, H. Yao, J. Hu, J. Zhou, L. Zhou and S. Wei, *Free Radical Biol. Med.*, 2018, **124**, 431–446.
40 H. Maeda, Y. Fukuyasu, S. Yoshida, M. Fukuda, K. Saeki, H. Matsuno, Y. Yamauchi, K. Yoshida, K. Hirata and K. Miyamoto, *Angew. Chem., Int. Ed.*, 2004, **43**, 2389–2391.
41 W. P. Li, C. H. Su, Y. C. Chang, Y. J. Lin and C. S. Yeh, *ACS Nano*, 2016, **10**, 2017–2027.
42 B. Liu, S. Liang, Z. Wang, Q. Sun, F. He, S. Gai, P. Yang, Z. Cheng and J. Lin, *Adv. Mater.*, 2021, **33**, 2101223.
43 J. Tang, H. Zhou, J. Liu, J. Liu, W. Li, Y. Wang, F. Hu, Q. Huo, J. Li, Y. Liu and C. Chen, *ACS Appl. Mater. Interfaces*, 2017, **9**, 23497–23507.
44 E. F. Garner and E. A. Beierle, *Cancers*, 2016, **8**, DOI: 10.3390/cancers8010005.
45 J. A. Joyce and D. T. Fearon, *Science*, 2015, **348**, 74–80.
46 D. Wang, J. Zhou, R. Chen, R. Shi, G. Xia, S. Zhou, Z. Liu, N. Zhang, H. Wang, Z. Guo and Q. Chen, *Biomaterials*, 2016, **107**, 88–101.
47 J. Wang, Y. Chen, B. Chen, J. Ding, G. Xia, C. Gao, J. Cheng, N. Jin, Y. Zhou, X. Li, M. Tang and X. M. Wang, *Int. J. Nanomed.*, 2010, **5**, 861–866.
48 X. Song, X. Luo, Q. Zhang, A. Zhu, L. Ji and C. Yan, *J. Magn. Mater.*, 2015, **388**, 116–122.
49 Q. L. Jiang, S. W. Zheng, R. Y. Hong, S. M. Deng, L. Guo, R. L. Hu, B. Gao, M. Huang, L. F. Cheng, G. H. Liu and Y. Q. Wang, *Appl. Surf. Sci.*, 2014, **307**, 224–233.